Eccentricity effects of microhole arrays on drag reduction efficiency of microchannels with a hydrophobic wall

Cite as: Phys. Fluids **24**, 112004 (2012); https://doi.org/10.1063/1.4767539
Submitted: 01 August 2012 . Accepted: 12 October 2012 . Published Online: 26 November 2012

Navid Kashaninejad, Nam-Trung Nguyen, and Weng Kong Chan

Eccentricity effects of microhole arrays on drag reduction efficiency of microchannels with a hydrophobic wall

Navid Kashaninejad, Nam-Trung Nguyen,[a] and Weng Kong Chan
School of Mechanical and Aerospace Engineering, Nanyang Technological University, Singapore 639798

(Received 1 August 2012; accepted 12 October 2012; published online 26 November 2012)

This paper experimentally investigates the effects of microhole eccentricity on the slip lengths of Stokes flow in microchannels with the bottom wall made of microhole arrays. The wettability of such microhole structures fabricated by the replica molding of polydimethylsiloxane is first analyzed measuring both static and dynamic contact angles. Subsequently, the drag reduction performance of the microchannels with such hydrophobic microhole surfaces is evaluated. The results indicate that the impact of microhole eccentricity on drag reduction performance correlates well with the contact angle hysteresis rather than with the static contact angle. Furthermore, microhole arrays with large normalized width and zero eccentricity show the minimum contact angle hysteresis of 18.7°. In these microchannels, the maximum percentage increase in the relative velocity is 39% corresponding to a slip length of 2.49 μm. For the same normalized width, increasing the normalized eccentricity to 2.6 increases the contact angle hysteresis to 36.5° that eventually reduces the percentage increase in relative velocity and slip length down to 16% and 0.91 μm, respectively. The obtained results are in qualitative agreement with the existing theoretical and numerical models. These findings provide additional insights in the design and fabrication of efficient micropatterned channels for reducing the flow resistance, and leave open questions for theoreticians to further investigate in this field. © *2012 American Institute of Physics*. [http://dx.doi.org/10.1063/1.4767539]

I. INTRODUCTION

Microchannel is a basic component in drug delivery devices, micro-electro-mechanical-systems (MEMS), and lab-on-a-chip systems. However, as the size of the channel reduces, the flow resistance becomes higher. Therefore, active and passive techniques to minimize the frictional drag in microchannels are extremely important. One of the passive techniques to decrease the flow frictional resistance is to pattern the microchannels with microstructured surfaces such as microgroove/rib and micropost/hole arrays to reduce the effective solid-liquid contact area. In such microchannels, the liquid is in contact with the periodic no-slip and shear-free regions, as shown in Fig. 1(a). Thus, the classical no-slip boundary condition (BC) is replaced by an effective slip velocity. The validity of this assumption was verified theoretically,[1–3] experimentally,[4–6] and numerically[7–9] in the literature.

Watanabe *et al.*[10] used low-energy surfaces to reduce the drag of laminar flows of Newtonian fluids. A reduction of drag of 14% was observed for water flowing in a circular pipe with a diameter on the order of several millimeters. Ou *et al.*[4] systematically fabricated different hydrophobic surfaces from silanized silicon whose static contact angles were in the range of 130° to 174°, and the contact angle hysteresis was more than 25°. They reported a slip length up to 25 μm on these surfaces. Numerous studies were conducted to investigate the influence of different parameters of superhydrophobic surfaces on drag reduction. More details on these works were recently reviewed.[11–13]

[a] Author to whom correspondence should be addressed. Electronic mail: mntnguyen@ntu.edu.sg.

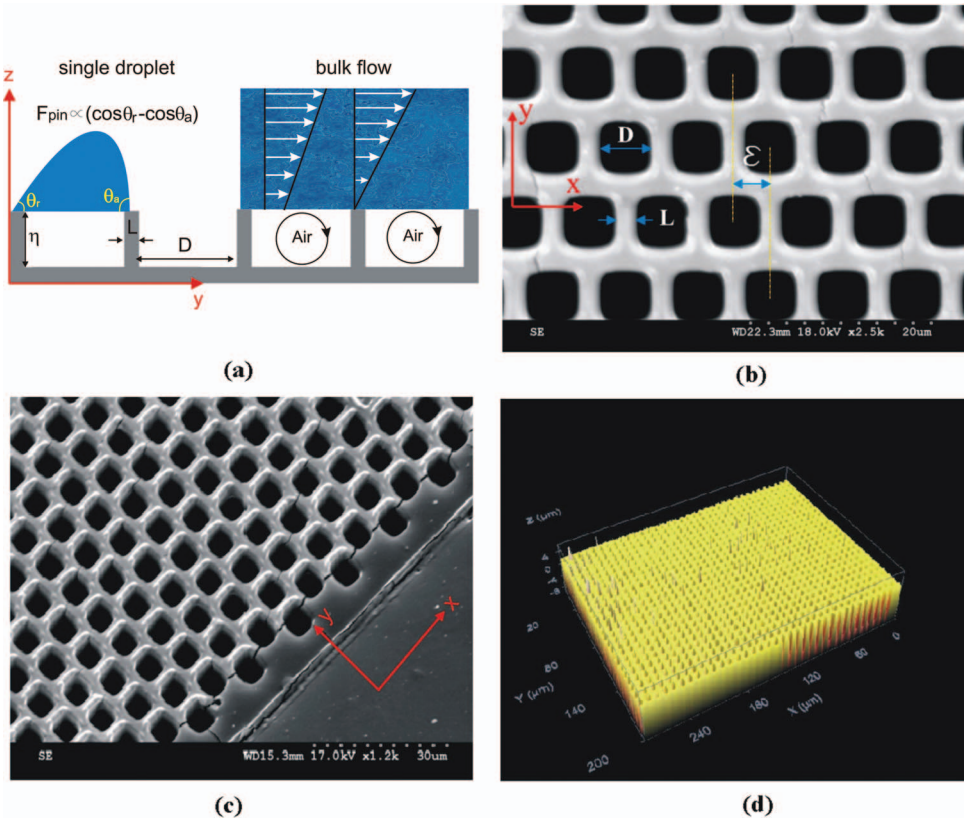

FIG. 1. Characteristics of the fabricated microholes in PDMS: (a) geometric parameters of the microholes reported in the literature. Also, the general conditions of single droplet and bulk flow near such surfaces are illustrated. (b) and (c) SEM images of the fabricated microholes and the definition of the eccentricity ε. (d) Confocal microscopic image of the microhole to measure the depth η.

In the literature, the effects of geometric parameters of microstructures such as those shown in Fig. 1(a) on the slip length, b, are thoroughly investigated. Both analytical and experimental results suggest that the slip length should be independent of the microchannel height, and can have the form of $b = f(\phi_g, \mathcal{L})$, where ϕ_g is the gas area fraction (shear-free region) and $\mathcal{L}$ is the spatial period of the microstructures ($\mathcal{L} = L + D$).[13] These parameters also affect the wettability of the surface.[14] For instance, if the spacing of a micropost array is large, liquid may penetrate into the cavities and the wetting condition shifts from the so-called Cassie-Baxter state[15] into the Wenzel[16] state leading to a decrease in the slip length. Therefore, parameters influencing the surface wettability conditions can subsequently affect the slip length and the bulk flow resistance. In addition, pinning of the droplet to the surface heterogeneities may also affect the bulk flow friction factor. This pinning force, F_{pin}, acting like a frictional resistance, is related to the advancing, θ_a, and receding, θ_r, contact angles of the single droplet, $F_{pin} \propto (\cos\theta_r - \cos\theta_a)$, as shown in Fig. 1(a). Therefore, it seems that wetting conditions of the microstructured surfaces can greatly influence the slip flow. Recently, we[17] introduced another important geometrical parameter of the micropattern termed as eccentricity, ε. Changing the eccentricity of the microstructures may affect the shape of the three-phase contact line, and subsequently influence both static and dynamic contact angles. This parameter is illustrated schematically in Fig. 1(b) for the periodic array of microholes investigated in this paper.

Wettability, and consequently, slip length are also functions of the shape of microstructured surfaces. Aside from random roughness structures,[18] previous works showed different values of slip length for flow in different directions (parallel or perpendicular) through microgrooves, microribs,[19] microposts, and microholes.[20,21] These results suggest that slip length may also be a function of the microhole eccentricity. To the best knowledge of the authors, the effect of microhole eccentricity

TABLE I. Geometrical parameters of the fabricated PDMS square microholes ($\eta = 10\,\mu m$).

$L(\mu m)$	$D(\mu m)$	$\varepsilon(\mu m)$	D^*	ε^*
1.5	7	0, 2, 4, 6	4.6	0, 1.3, 2.6, 4
2.5	6	0, 2, 4, 6	2.4	0, 0.8, 1.6, 2.4

on static/dynamic contact angles as well as bulk frictional flow resistance has not been investigated in the literature, and is the main objective of the present paper. Periodic microhole arrays in polydimethylsiloxane (PDMS) are designed and fabricated for two normalized widths while their normalized eccentricities are varied systematically. First, static and dynamic wetting conditions of these microhole structures are investigated. Then, the drag reduction performance of the microchannels made of such hydrophobic microhole surfaces is evaluated. The obtained results are discussed in terms of relative velocity increase and the effective slip length, and compared with the theoretical and numerical data.

II. EXPERIMENTAL METHODS

A. Design of microhole structures

Wetting condition of the microhole arrays differs from those of micropillar morphology reported throughout the literature. On the one hand, the three-phase contact line shape on the microhole configuration is real and continuous,[22] which may increase the possibility of droplet pinning.[23] On the other hand, subject to the bulk flow, the confined air inside the microhole features resists the invading water, and thus the Cassie-Baxter state becomes stable.[24] Therefore, it is of great interest to investigate the drag-reducing performance of such configurations. To this aim, the bottom wall of the channel was made of a periodic array of square microholes, Figs. 1(a)–1(d). The geometrical parameters of the microhole arrays, width D, spacing L, and eccentricity ε, are illustrated in Figs. 1(a) and 1(b). To minimize the amount of experimental data, all these parameters are normalized with respect to the spacing L. Also, normalized eccentricity $\varepsilon^* = \varepsilon/L$ is varied systematically at two ranges of normalized microhole width $D^* = D/L$ of 2.4 and 4.6, respectively. The detailed geometric values of the fabricated microhole surfaces are listed in Table I.

B. Fabrication of the microhole morphologies as the channel wall

Following a standard photolithography with AZ4620 positive photoresist and deep reacting ion etching (DRIE) processes, micropillars were first fabricated on the silicon wafers. The details of the fabrication technique were reported in our previous publication.[17] Here, micromolding technique was used to transfer the pillar geometries and form the microhole features on PDMS. Prepolymer (Sylgard 184, Dow Corning) was mixed with its curing agent in a ratio of 10:1 (w/w) and degassed in a vacuum pump for one hour. The cross-linked PDMS was carefully poured into the silicon master mold and baked in an oven for two hours at 65 °C. After peeling off the PDMS, the microholes were formed. To facilitate the peeling off process, the surface of the silicon wafer was treated with trichloromethylsilane (TCMS, Sigma Aldrich) as the releasing agent. The SEM images of these microhole morphologies are shown in Figs. 1(c) and 1(d).

C. Wettability analysis of the microhole array

To quantify the wettability of the fabricated microhole surfaces, an optical tensiometer (Theta Attension, BiolinScientific, Finland) was used. Since changing the eccentricity of the microhole arrays may change the anisotropy of the surface, all the contact angles were measured along a single viewing direction, y. To ensure the spherical shape of the droplet, the maximum volume of the droplet was selected to be 15 μL corresponding with the Bond number of 0.31. To measure the static contact angle, a small volume of de-ionized (DI) water ($V = 5\,\mu$L) was placed carefully on

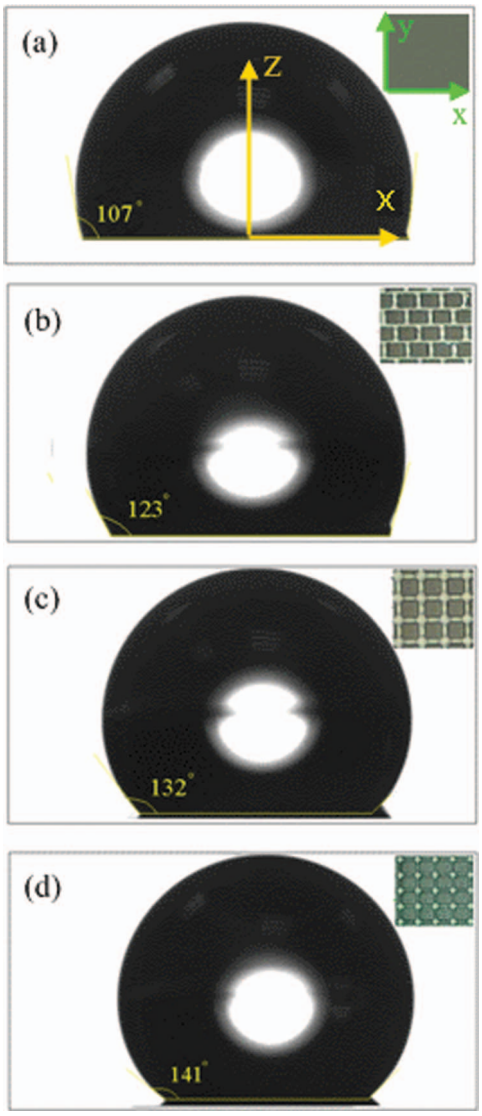

FIG. 2. Static contact angle variations with different geometric parameters of the microholes. (a) Contact angle on smooth PDMS. (b) Contact angle on microhole PDMS with D^*, $\varepsilon^* = 2.4$ (general effect of microhole arrays). (c) Contact angle on microhole PDMS with $D^* = 2.4$, $\varepsilon^* = 0$ (effect of decreasing ε^*). (d) Contact angle on microhole PDMS with $D^* = 4.6$, $\varepsilon^* = 0$ (effect of increasing D^*).

the surface of each sample. When the droplet has stabilized, its image was captured and analyzed using the tensiometer software. The static contact angles of different microhole arrays are shown in Fig. 2.

Since the contact line shape is continuous on microhole geometry, the hysteresis of the contact angle is not negligible. The static contact angle cannot quantify the wettability of the surface because its value lies between those of the advancing and receding contact angles. To measure the dynamic contact angle, the so-called embedded needle technique was used as recommended by the supplier for superhydrophobic surfaces. To measure the advancing contact angle, the droplet volume was increased very slowly at a rate of 0.05 μL/s from its initial volume of 2 μL to the maximum volume of 10 μL. The images were recorded with 0.6 frames per second. Subsequently, the volume was increased to 15 μL and then decreased back to its initial volume of 10 μL. Maximum achievable contact angle during this process was recorded as the advancing contact angle. The reverse process was performed to measure the receding contact angle. The pixel error of the tensiometer is reported

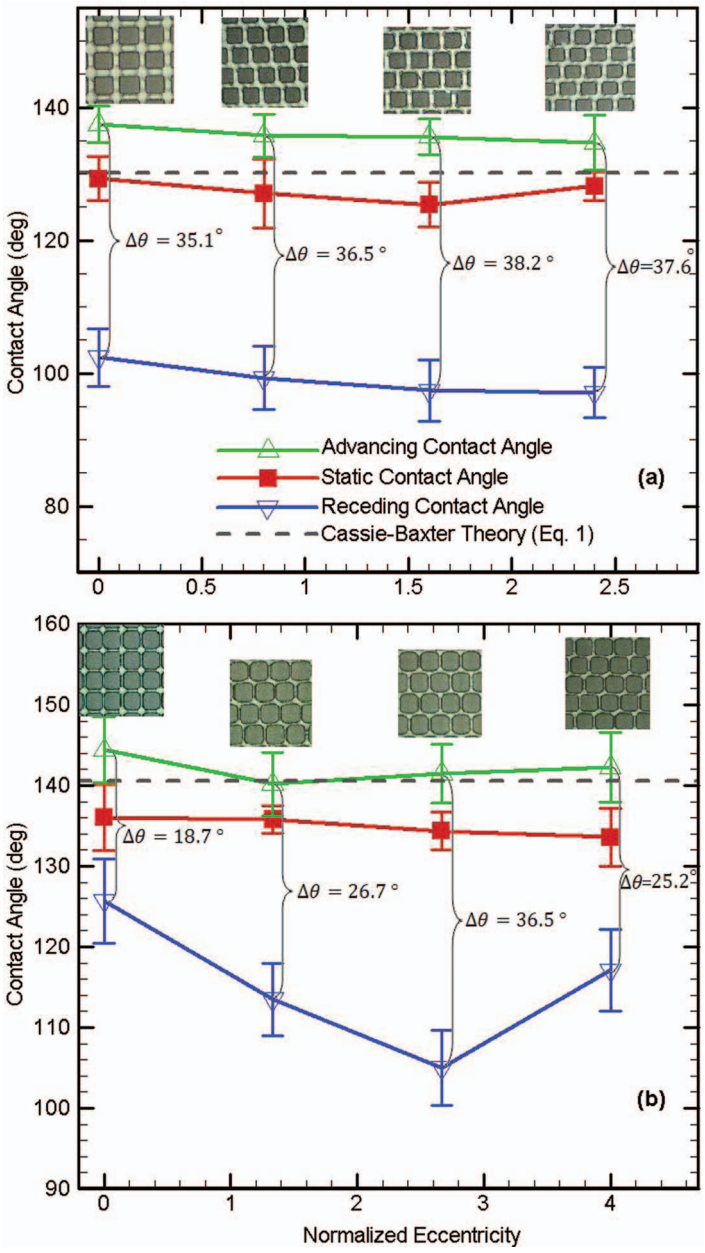

FIG. 3. Experimental results of static, advancing, and receding contact angles as a function of microhole normalized eccentricity. (a) $D^* = 2.4$. (b) $D^* = 4.6$.

to be around 0.1°. All measurements were conducted at least six times at different locations on the sample, and the results are shown in Figs. 3(a) and 3(b). The reported contact angles are the average values with the error bars indicating the standard deviations from the data set. The contact angle hysteresis $\Delta\theta$ in Figs. 3(a) and 3(b) is the difference between the advancing and receding contact angles. The static Cassie-Baxter contact angle, θ_{CB}, on heterogeneous surface was theoretically obtained[15]

$$\cos\theta_{CB} = \left(1 - \phi_g\right)\cos\theta_{smooth} + \phi_g \cos\pi, \tag{1}$$

where θ_{smooth} and π are contact angles on smooth solid and gas portions, respectively. Considering the present microhole arrays with $\phi_g = D^2/(D+L)^2$ and the measured smooth contact angle on PDMS,

$\theta_{smooth} = 107^\circ$, the static contact angles on such microhole morphology are calculated and compared with the experimentally obtained static and dynamic contact angles in Fig. 3. It should be noted that the effective contact angle can be compared with Cassie-Baxter equation since the continuum approach is valid. That means, the drop size ($\sim$1 mm) is much larger than surface heterogeneities ($\sim 10\,\mu$m).

First, the results indicate that Cassie-Baxter contact angle can predict reasonably well the average static and advancing contact angles on microhole arrays independent of the microhole eccentricity. However, the receding contact angle and subsequently the contact angle hysteresis $\Delta\theta$ cannot be predicted by Cassie-Baxter theory. Second, the results suggest that static contact angle increases by increasing the normalized microhole width D^* while changing the microhole eccentricity does not affect the contact angle significantly. However, contact angle hysteresis can be altered by changing the microhole normalized eccentricity ε^*. In particular, for the case of $D^* = 4.6$ increasing ε^* to 2.6 increases the contact angle hysteresis from 18.7° to 36.5°, and consequently affects the resistant force and mobility of a sessile droplet. In addition, the static and dynamic contact angles of $D^* = 2.4$ and $\varepsilon^* = 0.8$, 2.4 as well as $D^* = 4.6$ and $\varepsilon^* = 1.3$, 4.0 are very similar, which may be attributed to the periodicity of the microhole arrays. Dependency of the contact angle hysteresis on microhole eccentricity can be explained by the shape of the three-phase contact line on microhole configurations. For small values of D^*, the contact angle hysteresis has a large value of more than 35°, implying that the contact line is continuous and pinned to the edge of the solid parts. In this case, changing the microhole eccentricity does not significantly affect the shape of contact line and thus $\Delta\theta$ is almost independent of the microhole eccentricity. However, by increasing D^*, the shear-free portion increases improving the mobility of the droplet with a contact angle hysteresis as low as 18.7°. The decrease in contact angle hysteresis implies that the three-phase contact line shape is rather discontinuous.[23] In this case, changing the microhole eccentricity has the higher impact. This finding emphasizes the important role of contact line topology on wettability condition, which is not included in the Cassie-Baxter equation.

D. Fabrication of superhydrophobic microchannels

The fabricated microhole surfaces were implemented as the bottom wall of microchannels to investigate the pressure drop performance under the varying microhole normalized eccentricities and widths. Serpentine microchannels were fabricated via soft lithography followed by replica molding as summarized in Figs. 4(a)–4(d). First, the channels were designed with AutoCAD software. For calibration purpose, precise ruler marks at intervals of 250 μm were indicated next to the measurement channel. The serpentine microchannel was designed with 11 straight channels and 18

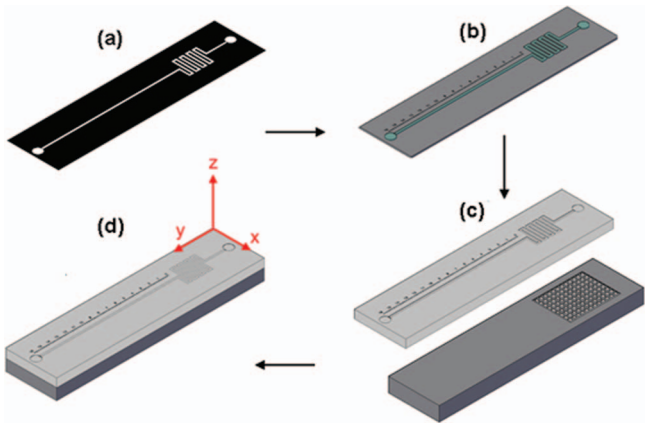

FIG. 4. Microchannel fabrication process: (a) channel features designed on plastic mask for photolithography; (b) master mold of SU-8 on a silicon wafer; (c) microchannel features after PDMS replica molding (top) along with the microhole arrays (bottom); (d) sealed microchannel after inlet/outlet punching and bonding the top and bottom walls.

bends forming a total length $L_{tot} = 41.25$ mm and a width of $w = 220\,\mu$m, Fig. 4(a). As the next step, SU-8 photoresist was first spin coated on an ultrasonically cleaned silicon wafer. Finally, the UV exposure time determined the thickness of the SU-8.

To highlight the drag reducing effect, the height of the microchannel or the SU-8 thickness was selected to be $20\,\mu$m. After post baking the wafer for 10 min. at 85°C. the SU-8 thickness was measured using a stylus profilometer (Dektak Brand) to be $17.95 \pm 0.05\,\mu$m, Fig. 4(b). Following the same procedure for PDMS replica molding, the channel features were transferred into PDMS, Fig. 4(c). Both PDMS substrates were thoroughly soaked in DI water and cleaned with ultrasound cleaner for 30 min. Then, they were preheated in an oven for another 15 min. at 80°C and finally bonded together with the help of a 30-seconds exposure to oxygen plasma. To enhance the bonding quality, the device was heated in the oven for 2 h at 80°C. However, because of the ragged surface of the microholes, oxygen plasma bonding only sealed the smooth part of the PDMS channel. To bond the microhole channel irreversibly, a thin intermediate layer of dilute PDMS was used as an adhesive.[25] First, 2 mL PDMS mixture was dissolved in tert-Butanol with 85% (w/w) ratio. The solution was then spin-coated on a 2.4 cm × 5 cm clean glass substrate in two steps: first at 550 rpm for 6 s to evenly spread the PDMS-tertButanol solution, then the speed was increased to 1200 rpm and maintained for 60 s. Subsequently, the PDMS slab with microchannels was gently placed in contact with the PDMS coated substrate. After pressing the channel slab on the PDMS slab with microhole patterns and baking for 2 h at 65 °C, an irreversible bond was formed and the microchannels walls were effectively sealed, Fig. 4(d).

E. Experimental apparatus for pressure-velocity measurement

To investigate the effect of geometric parameters of the microholes, average velocity of the DI water flow was recorded as a function of the hydrostatic pressure. The actual as well as schematic experimental setups are shown in Figs. 5(a) and 5(b). To generate the small, yet stable flow rate, a DI water reservoir was mounted on a precise height gauge (with 0.01 mm accuracy). Different values of hydrostatic pressure were obtained by altering the effective gap (denoted as H_{static} in Fig. 5) from 5 cm to 15 cm. Moreover, to measure the relative gap between the DI water reservoir and

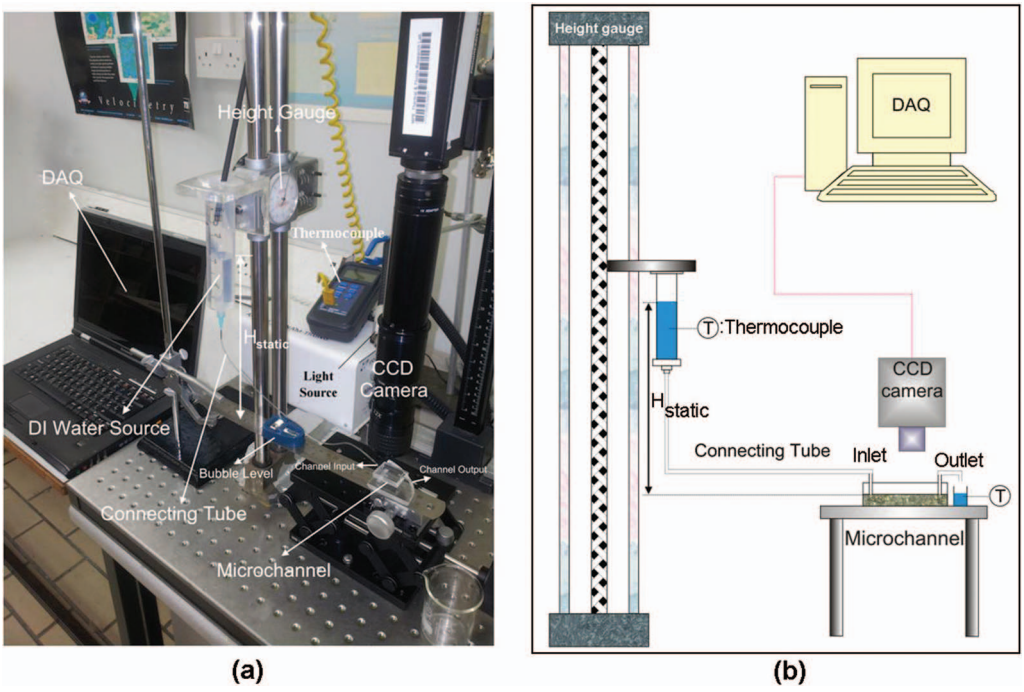

FIG. 5. (a) Actual experimental test rig. (b) Schematic illustration of the set up.

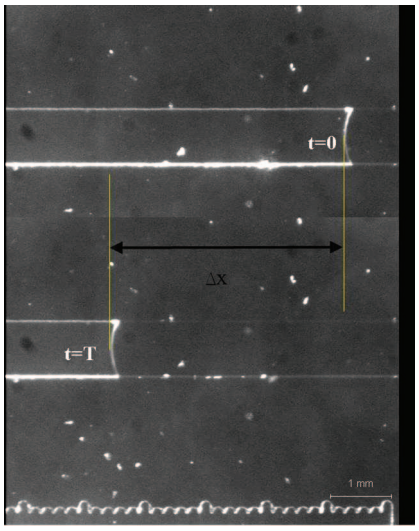

FIG. 6. Illustration of the method used to measure the average velocity of the microchannels.

the channel inlet more precisely, an adjustable ruler and a bubble leveler were used. A thermocouple was used to measure the temperature change on the DI water during the experiment. It was observed that the temperature difference between the channel inlet and outlet was less than 0.2°C. Hence, the properties of the DI water such as dynamic viscosity and density were assumed to be constant at an average temperature of $\bar{T} = 21.9$°C. As the working liquid passed through the straight measurement channel with the ruler marks, a CCD camera was used to monitor the flow in a known time $T = n_t/f_r$, where n_t is the total number of images (usually 143) and f_r is the frame rate. Image processing for evaluating the flow displacement $\Delta y \pm 50\ \mu$m was conducted using Image-Pro Plus software, Fig. 6. The average velocity was subsequently calculated. The channels are coded as ABC-D-E, where AB shows the channel materials, C indicates whether the bottom wall of the channel is smooth (S) or patterned with microholes (H), and D and E correspond to the microhole normalized width and eccentricity, respectively. For instance, PPH-D2.4-E1.6 means PDMS/PDMS (PP) microchannel fabricated from microhole bottom wall with $D^* = 2.4$ and $\varepsilon^* = 1.6$. Accordingly, nine different microchannels were tested in this experiment under the identical conditions.

1. Experimental uncertainties of the data

In our present work, the total experimental uncertainty, U_{x_i}, of the independent variables x_i, was calculated from the following relationship:[26]

$$U_{x_i} = 2\sqrt{\left(\frac{\epsilon_b}{2}\right)^2 + \left(\frac{\epsilon_s}{\sqrt{N}}\right)^2}, \tag{2}$$

where ϵ_b is the bias error due to the limited accuracy of the measuring devices, is ϵ_s the standard deviation as a result of random error during the experiment, and N is the number of the samples. Here, the bias error of the pressure measurement is negligible because the maximum relative error of the hydrostatic height is $\pm 0.02\%$ corresponding to a minimum height of $H_{static} = 50$ mm. Also, the bias error of the velocity measurement is only related to the error in measuring the displacement $\Delta y \pm 0.05$ mm since the time is accurately determined by the number of images and the frame rate of the CCD camera. Thus, to decrease the relative importance of this error, the maximum allowable value of Δy (more than 2 mm but less than 6 mm) was recorded by adjusting the frame rate of the CCD camera. Accordingly, the maximum relative error of the measured velocity was found to be $\pm 2\%$.

Moreover, the experimental error U_y of the dependent variable y, calculated from the directly measured quantities, i.e., $y = f(x_i)$, was found based upon the error propagation formula given by

$$U_y = \sqrt{\sum_{i=1}^{n} \left(\frac{\partial f}{\partial x_i} U_{x_i} \right)^2}. \tag{3}$$

Throughout the present paper, the uncertainty for each variable is represented by the corresponding error bar in the related figures, and detailed calculations are provided in Appendixes A and C.

2. Data analysis and pressure loss calculation

Since the maximum Reynolds number Re in this work was less than 0.035, the effect of inertia was negligible, and Stokes flow was dominant. Considering the microchannel with a finite width (w) to height (h) aspect ratio, $\alpha = w/h$, velocity distribution u can be found by solving the Stokes equation

$$\frac{\partial^2 u}{\partial x^2} + \frac{\partial^2 u}{\partial z^2} = \frac{\nabla P}{\mu_w}, \tag{4}$$

where x and z are the cross-section coordinates of the microchannel, ∇P is the pressure gradient in the streamwise direction y, and μ_w is the dynamic viscosity of the fluid. Considering the no-slip BCs on the channel walls and using eigenfunction expansion technique, it can be shown that the flow average velocity by considering the side wall effects, $\bar{u}_{2D}$, becomes[27]

$$\bar{u}_{2D} = \bar{u}_{H-P} C(\alpha), \tag{5}$$

where $\bar{u}_{H-P} = -\frac{h^2 \nabla P}{12 \mu_w}$ is the classical Hagen-Poiseuille (H-P) average velocity with no slip BCs, and $C(\alpha) = \frac{48\alpha^2}{\pi^6} \sum_{n=1}^{\infty} \sum_{m=1}^{\infty} \frac{[1-\cos m\pi]^2 [1-\cos n\pi]^2}{m^2 n^2 (m^2+\alpha^2 n^2)}$ is the additional term resulting from the finite aspect ratio.

Figure 7 shows the comparison of experimental and analytical values of average velocity as a function of hydrostatic pressure for smooth microchannels. As the results suggest, the obtained

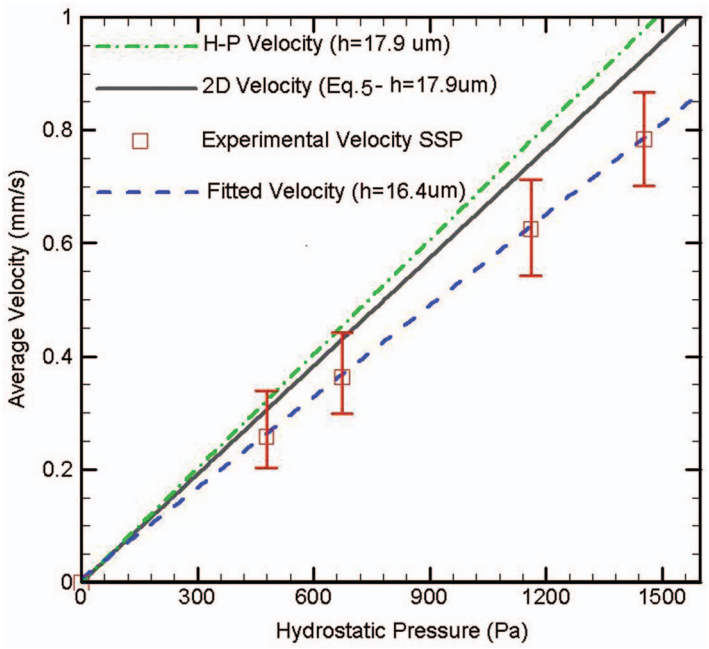

FIG. 7. Comparison of experimental and analytical values of average velocity as a function of hydrostatic pressure for smooth microchannel (head losses decrease the effective channel height).

analytical formula can better predict the experimental data because the aspect ratio of the channel is small. In this case, considering the effect of side walls makes the analysis more realistic. The pressure drop was calculated based on the hydrostatic height, H_{static}, i.e., $\Delta P = P_{in} - P_{out} = \rho g H_{static}$. However, there might be some head losses along the channel, which can reduce H_{static},

$$H_{loss} = H_{l,in} + H_{l,out} + H_{l,dev} + H_{l,tube} + H_{l,minor} + H_{l,ev}, \tag{6}$$

where H_{loss} is the total head loss, $H_{l,in}$, $H_{l,out}$ are entrance and exit head losses, respectively, $H_{l,dev}$ is the head loss of developing region, $H_{l,tube}$ is the head loss of the connecting tubes, $H_{l,minor}$ is the minor loss due to the meandering nature of the channel as well as the fittings, and $H_{l,ev}$ is the head loss as a result of electroviscous effect. Since we intended to compare the performance of the microhole fabricated microchannels, rather than computing these losses, the experimental data of the smooth PDMS channel was considered as a reference to calibrate the effective height of the channel to indirectly find these losses. As shown in Fig. 7, effective channel height of $h = 16.4\,\mu$m can fit the experimental data reasonably well. Therefore, the total loss can reduce the height of the channel by $1.5\,\mu$m.

III. RESULTS AND DISCUSSIONS

A. Raw experimental data of pressure-velocity measurement

The experimental results of the average velocity versus hydrostatic pressure of the channels with smooth and microhole patterns are presented in Figs. 8(a) and 8(b). The results suggest that the average velocity at the same hydrostatic pressure is higher in microhole channels as compared to the smooth one. Furthermore, the geometric parameters of the microhole arrays can also affect the values of the velocity and pressure drop.

B. Percentage increase of velocity in the microhole channels

To further clarify the results, percentage increase in velocity of the microhole channels at the given pressure, Λ, is defined as

$$\Lambda = \frac{\bar{u}_{microhole} - \bar{u}_{smooth}}{\bar{u}_{smooth}} \times 100\%, \tag{7}$$

where $\bar{u}_{microhole}$ and $\bar{u}_{smooth}$ are the average velocities of the microchannel with microholes and smooth bottom walls, respectively. Figures 9(a) and 9(b) show the variations of this parameter as a function of hydrostatic pressure at different values of normalized width and eccentricity. The uncertainty calculation of Λ is presented in Appendix A, and its corresponding values are shown by error bars in Figs. 9(a) and 9(b).

The results demonstrate that patterning the bottom channel wall with microhole arrays increases the average velocity at the same hydrostatic pressure as compared to the smooth channel wall. Figure 9(a) depicts the percentage increase for channels with $D^* = 2.4$. The average velocity can increase up to 17%, and it is almost independent from the values of the eccentricity. However, Fig. 9(b) reveals that the drag reduction performance of the microchannels may be strongly affected by changing the eccentricity as well. As in the case of $D^* = 4.6$ and $\varepsilon^* = 2.6$, the lowest increase in the average velocity was observed.

To justify the observed trend of the increase in velocity, the drag reduction performance of the microchannels is plotted as a function of the microhole eccentricity, Fig. 10.

Figure 10 illustrates that the average percentage increase of the velocity of the microhole channels can be controlled by changing both width and eccentricity of the microhole. In particular, for $D^* = 4.6$ and $\varepsilon^* = 0$ the average velocity increases up to 39%. While at the same D^*, increasing the normalized eccentricity to 2.6 lowers the average Λ down to 16%. At lower values of D^*, microchannels drag-reducing ability seems to be independent of the microhole eccentricity. In this case, the average values of Λ are around 15%. Generally, it can be concluded that at the same microhole eccentricity, channels with larger normalized width have higher values of Λ. Importantly,

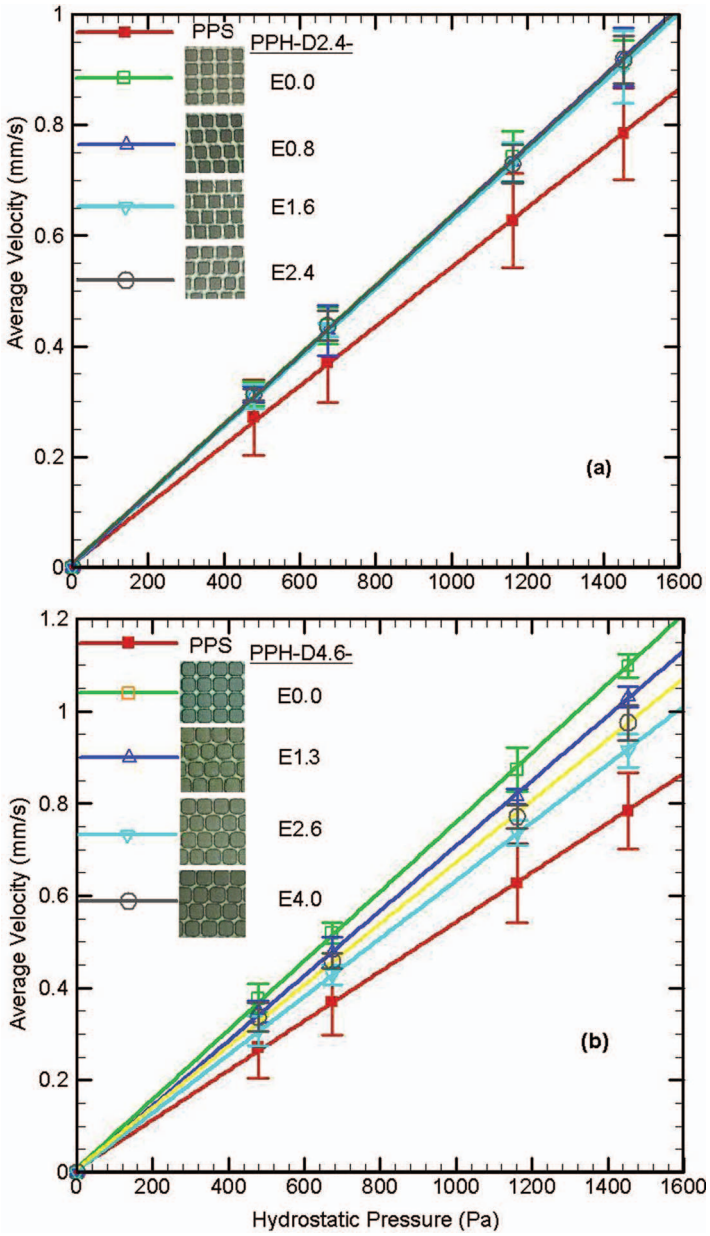

FIG. 8. Average velocity as a function of hydrostatic pressure for microchannels at different values of microhole eccentricity. (a) $D^* = 2.4$. (b) $D^* = 4.6$. For comparison, the experimental data of a smooth channel with the same channel height ($h = 17.9\ \mu m$) are also presented.

at the same normalized width, increasing the eccentricity decreases the average values of Λ. Although this behavior differs from the trend of the static contact angle observed on these microhole surfaces, it correlates well with the trend of the contact angle hysteresis. Contact angle hysteresis directly relates to the critical line force caused the droplet to roll on a solid surface.[13] In other words, as the contact angle hysteresis decreases, the droplet moves faster on the surface. Also, as mentioned before and shown in Fig. 1(a), the pinning force of the droplet is directly proportional to the difference of the cosines of the advancing and receding contact angles. Thus, surfaces with lower contact angle hysteresis induce fewer pinning forces. Hence, the drag reducing efficiency of the bulk flow should be proportional to the contact angle hysteresis, which is in good agreement with our present results. Therefore, we can conclude that the static contact angle alone is unable to predict the drag reduction

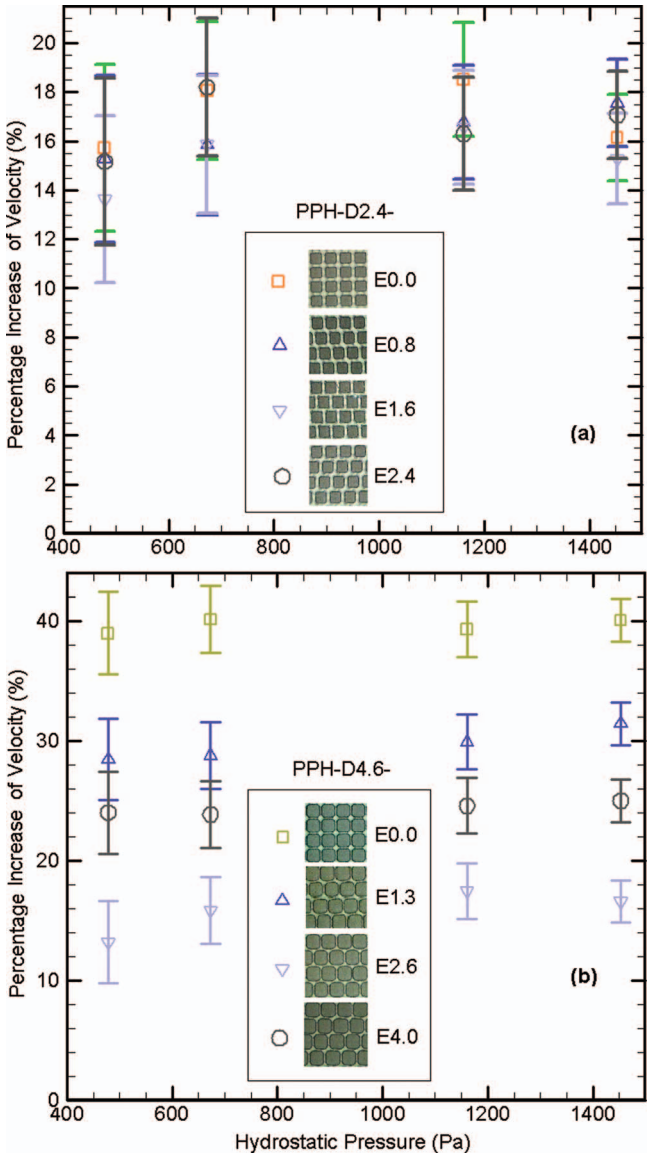

FIG. 9. Percentage increase in the relative velocity Λ vs. hydrostatic pressure for the microchannels at different values of microhole eccentricity. (a) $D^* = 2.4$. (b) $D^* = 4.6$.

ability of microchannels patterned with microholes. Advancing and receding contact angles should also be quantified to further understand the trend of drag reduction.

C. Experimental slip length

Frictional drags in microchannels can be smaller than those in the macrochannels mainly as a result of the slip between the liquid and the solid surface. It is generally assumed that the slip velocity at the solid wall is proportional to the shear rate, and the constant of proportionality is called slip length b. Here, we assume that intrinsic slip on the smooth PDMS top wall is negligible, $b^+ = 0$. Moreover, by denoting $\beta = b^-/h$ as the effective normalized slip length of the bottom wall of the channel, the average slip velocity $\bar{u}_{slip}$ can be written as (detailed derivation is presented in

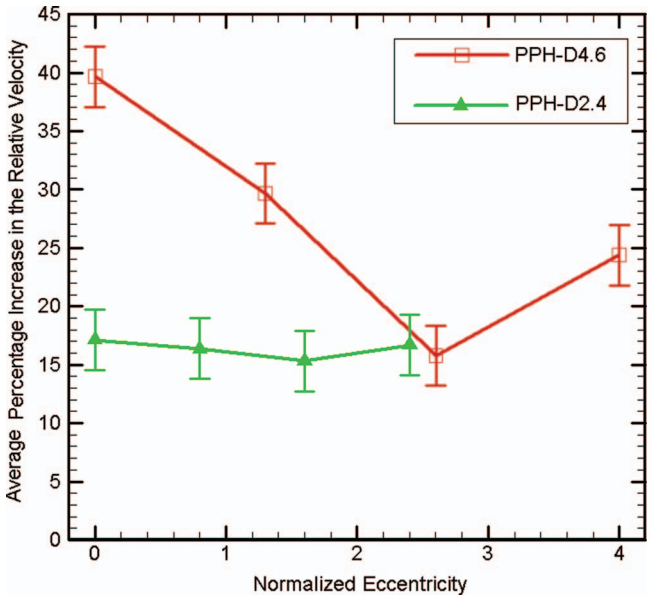

FIG. 10. Average Λ as a function of the microhole normalized eccentricity ε^* for different values of D^*.

Appendix B)

$$\bar{u}_{slip} = \bar{u}_{H-P}\left(\frac{1+4\beta}{1+\beta}\right). \tag{8}$$

The normalized experimental effective slip length, β_{exp}, then becomes

$$\beta_{exp} = \frac{\bar{u}_{slip}/\bar{u}_{H-P} - 1}{4 - \bar{u}_{slip}/\bar{u}_{H-P}}. \tag{9}$$

In this work, β_{exp} was obtained by considering $\bar{u}_{slip} = \bar{u}_{microhole}$ and $\bar{u}_{H-P} = \bar{u}_{smooth}$.

D. Theoretical slip length

For superhydrophobic surface containing 1D periodic BCs of shear-free and no-slip patterns, the following analytical formula is derived:[1,3]

$$\beta_{th,1D,\|[\perp]} = \frac{1}{[2]\pi h}\mathcal{L}\ln(\sec\left(\delta\frac{\pi}{2}\right)), \tag{10}$$

where $\beta_{th,1D,\|[\perp]}$ is the normalized (with respect to channel height h) slip length of the 1D strip patterns parallel [perpendicular] to flow direction, and $\delta = D/\mathcal{L}$ is the shear-free fraction. If the gas area fraction is large, 1D periodic patterns can be considered as the limiting case for microhole arrays. Ybert *et al.*[21] proposed a scaling law for the effective slip length of the 2D micropost arrays in terms of the geometry-dependent coefficients. These coefficients were numerically determined by Cheng *et al.*[20] Similarly, here it is hypothesized that the normalized theoretical slip length of the 2D microhole, $\beta_{th,2D}$, can be scaled as

$$\beta_{th,2D} \sim \frac{\mathcal{L}}{h}\ln(\sec\left(\phi_g\frac{\pi}{2}\right)) \rightarrow \beta_{th,2D} = \mathcal{A}\,\mathcal{L}\ln(\sec\left(\phi_g\frac{\pi}{2}\right)) + \mathcal{B}, \tag{11}$$

where $\mathcal{A}$ and $\mathcal{B}$ are the two normalized shape factors, which depend on the geometry of the microholes. These two free parameters are used to fit the experimental data as a result of the microholes with different values of eccentricity, and thus have no predictive capabilities. In Figs. 11(a) and 11(b), the experimental values of slip length β_{exp} from Eq. (9) are compared

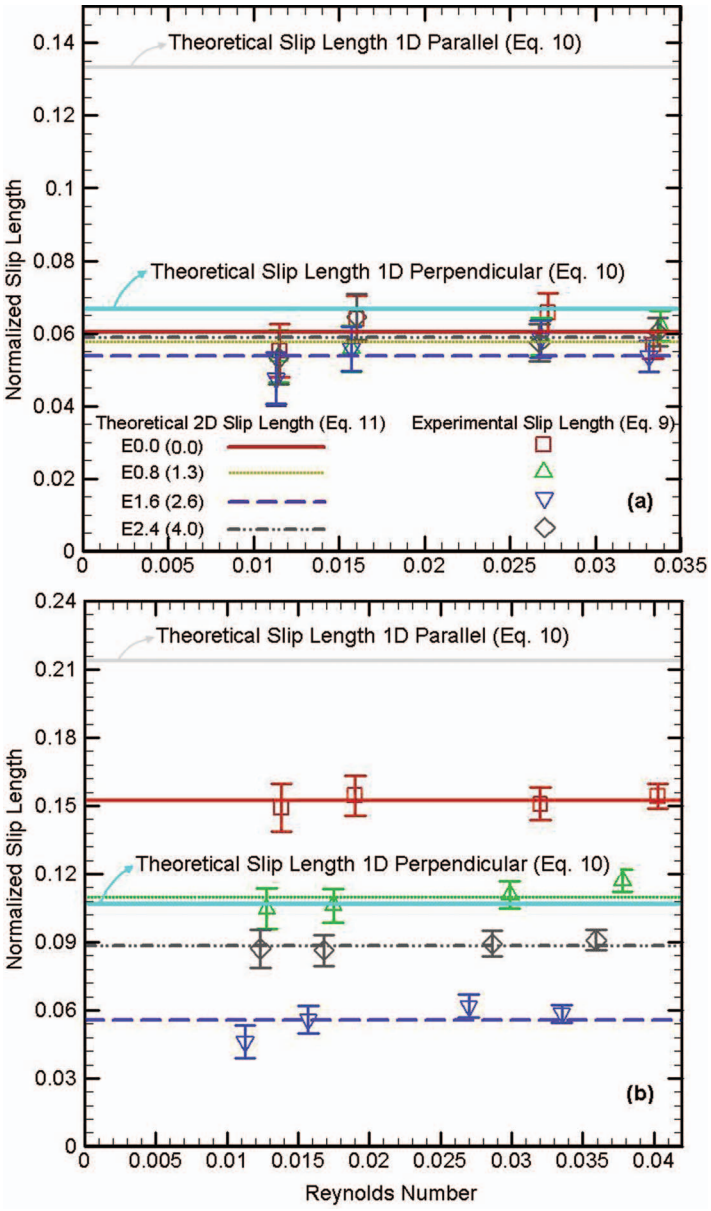

FIG. 11. Theoretical and experimental values of slip length as a function of Reynolds number for the microchannels at different values of microhole eccentricity: (a) $D^* = 2.4$. (b) $D^* = 4.6$.

graphically to the theoretical counterparts of $\beta_{th,1D,||[\perp]}$ and $\beta_{th,2D}$ predicted from Eqs. (10) and (11), respectively. The corresponding values of the shape factors $\mathcal{A}$ and $\mathcal{B}$ are listed in Table II.

Generally, the obtained results in Figs. 11(a) and 11(b) suggest that the theoretical slip length corresponding to the 1D strip patterns perpendicular to the flow direction (Eq. (10) with 1/2 factor) can be used well to predict the experimental results. Yet, the 1D parallel model overestimates the values of the experimental slip length. This observation is consistent with the reported results of Ybert *et al.*,[21] who stated that the flow over the microholes with low surface area fraction, i.e., $\phi_g \rightarrow 1$, should be similar to the 1D grooves perpendicular to the flow direction. In particular, for the case of microholes with $D^* = 4.6$, Eq. (11) with the shape factors listed in Table II can be used to predict the experimental values of slip length accurately, even as a function of microhole eccentricity.

TABLE II. Normalized shape factors corresponding to the normalized slip lengths in different configurations.

	1-D patterns parallel (perpendicular)	PPH-D2.4(4.6)-E0.0(0.0)	PPH-D2.4(4.6)-E0.8(1.3)	PPH-D2.4(4.6)-E1.6(2.6)	PPH-D2.4(4.6)-E2.4(4.0)
$\mathcal{A}$	0.0194 (0.0097)	0.028299	0.016037	0.00051239	0.0091044
$\mathcal{B}$	0 (0)	−0.0222	0.010847	0.052388	0.032306

Furthermore, Fig. 11(a) indicates that the values of slip length for microchannels with $D^* = 2.4$ are independent of the eccentricity in the investigated creeping regime. In this case, the slip length cannot exceed more than $b = 0.99\,\mu$m. However, results of Fig. 11(b) state that slip length can be reduced by changing the microhole eccentricity. In particular, slip length decreases from $b = 2.49\,\mu$m for $\varepsilon^* = 0$ to $b = 0.91\,\mu$m for $\varepsilon^* = 2.6$. This finding is in good agreement with the numerical simulations conducted by Koopaee *et al.*[28] They showed that the friction factor of aligned microposts, corresponding to $\varepsilon^* = 0$ in this study, is smaller than the staggered microposts, corresponding to $\varepsilon^* \neq 0$ in this study. Here, we observed that further increasing the eccentricity led to increasing the slip length as a result of periodicity of the patterns.

IV. CONCLUSIONS

In this paper, the effects of microhole eccentricity on drag reduction of Stokes flow through hydrophobic microchannels were investigated. The microhole patterns were fabricated by PDMS replica molding, and characterized by the measurement of both static and dynamic contact angles. It was found that wetting conditions can be controlled not only by changing the normalized widths, but also the eccentricities. Generally, increasing the microhole eccentricity increased the contact angle hysteresis. The effect of changing the eccentricity was more pronounced for large normalized width microhole arrays. In particular, for the case of $D^* = 4.6$, increasing ε^* from 0 to 2.6 increased the contact angle hysteresis from 18.7° to 36.5°. Dependency of the contact angle hysteresis on microhole eccentricity was explained by the shape of the three-phase contact line on microhole configurations. Subsequently, a series of experiments was performed for the pressure driven flow through these hydrophobic microhole channels, and drag reduction performance was evaluated. For microchannels with $D^* = 4.6$ and $\varepsilon^* = 0$, the average velocity increases up to 39% as compared to a smooth PDMS microchannel, with a corresponding slip length of 2.49 μm. For the same D^*, increasing the normalized eccentricity to 2.6 decreases the average percentage increase of the velocity Λ and the slip length to 16% and 0.91 μm, respectively. For a lower value of D^*, microchannels drag-reducing ability was independent from the microhole eccentricity. In this case, the average values of Λ were around 15%, and the corresponding slip length is less than 1 μm. These observations were consistent qualitatively with the analytical as well as numerical results reported previously in the literature. It should be emphasized here that although empirical formula, i.e., Eq. (11), was used to relate the slip length of microhole surfaces to the eccentricity of the patterns, it is expected that more experimental and theoretical works be conducted in near future to more stringently predict the effects of changing the microhole eccentricity on the contact angle hysteresis as well as slip length. In conclusion, the shape of three-phase contact line plays a crucial role for both single droplet wettability and bulk flow drag reduction performance, which can be controlled by changing both normalized width and eccentricity of the microholes.

APPENDIX A: UNCERTAINTY OF PERCENTAGE INCREASE OF VELOCITY

Generally, if a dependent variable z is a function of independent variables A and B, $z = z(A, B)$, and uncertainties of A and B, are denoted by ΔA and ΔB, respectively, then Δz, the uncertainty of z, becomes

$$\Delta z = \sqrt{\left(\frac{\partial z}{\partial A}\Delta A\right)^2 + \left(\frac{\partial z}{\partial B}\Delta B\right)^2}. \tag{A1}$$

Considering Eq. (7), and denoting $\bar{u}_{microhole} = A$, $\bar{u}_{smooth} = B$ and the percentage increase of velocity $\Lambda = z$, then Eq. (7) can be rewritten as $z = (A - B)/B$. Therefore,

$$\frac{\partial z}{\partial A} = \frac{1}{B} \quad ; \quad \frac{\partial z}{\partial B} = -\frac{A}{B^2}. \tag{A2}$$

Substituting Eq. (A2) in Eq. (A1) results

$$\Delta z = \frac{1}{B}\sqrt{\Delta A^2 + \left(\frac{A}{B}\right)^2 \Delta B^2}. \tag{A3}$$

By replacing A, B, z, the uncertainty of percentage increase of velocity, $\Delta\Lambda$, becomes

$$\Delta\Lambda = \frac{1}{\bar{u}_{smooth}}\sqrt{\Delta\bar{u}^2_{microhole} + \left(\frac{\bar{u}_{microhole}}{\bar{u}_{smooth}}\right)^2 \Delta\bar{u}^2_{smooth}}. \tag{A4}$$

The percentages of these uncertainties are shown by error bars in Fig. 9.

APPENDIX B: DERIVATION OF EXPERIMENTAL SLIP LENGTH

The general form of Newtonian Stokes liquid flow in a rectangular microchannel with a large aspect ratio consisting of two different walls with different wetting conditions is considered. Schematic view of such microchannel is illustrated in Fig. 12.

Considering fully developed laminar flow for Newtonian liquids with constant properties at low Reynolds number, Navier-Stokes equation can be simplified to Stokes equation

$$\frac{d^2u}{dz^2} = 1/\mu_w \nabla P \Rightarrow \frac{du}{dz} = 1/\mu_w \nabla P z + C_1 u(z)\, 1/2\mu_w \nabla P z^2 + C_1 z + C_2. \tag{B1}$$

Subject to Navier slip BCs at both channel walls

$$\begin{cases} u\,(z = +\mathrm{h}/2) = -b^+ \left.\dfrac{du}{dz}\right|_{z=+h/2} \\ u\,(z = -h/2) = b^- \left.\dfrac{du}{dz}\right|_{z=-h/2} \end{cases}. \tag{B2}$$

Upon imposing these BCs into Eq. (B1) and further simplifications, the general equation describing the average velocity can be obtained as

$$\bar{u}_{slip} = -1/\mu_w \nabla P[\frac{h^3 + 4h^2b^- + 4h^2b^+ + 12hb^+b^-}{12\,(h + b^+ + b^-)}]. \tag{B3}$$

Assuming $b^+ = 0$ and denoting $\beta = b^-/h$, the average slip velocity becomes

$$\bar{u}_{slip} = -\frac{h^2\nabla P}{12\mu_w}\left(\frac{1 + 4\beta}{1 + \beta}\right). \tag{B4}$$

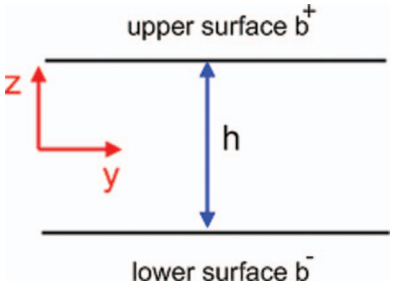

FIG. 12. Schematic view of the channel with different slip lengths on both walls.

Denoting $\bar{u}_{H-P} = -\dfrac{h^2 \nabla P}{12\mu_w}$, the relationship describing the normalized effective slip length β becomes the same as Eq. (9).

APPENDIX C: UNCERTAINTY OF EXPERIMENTAL SLIP LENGTH

Equation (9) can be written as $\beta_{exp} = \dfrac{\bar{u}_{slip} - \bar{u}_{H-P}}{4\bar{u}_{H-P} - \bar{u}_{slip}}$. Thus, by denoting $\bar{u}_{slip} = A$, $\bar{u}_{H-P} = B$, and $\beta_{exp} = z$, then this equation becomes

$$z = \frac{A - B}{4B - A}. \tag{C1}$$

Therefore

$$\frac{\partial z}{\partial A} = \frac{3B}{(4B - A)^2} \quad ; \quad \frac{\partial z}{\partial B} = \frac{-3A}{(4B - A)^2}. \tag{C2}$$

Substituting Eq. (C2) in Eq. (A1) results

$$\Delta z = \frac{3}{(4B - A)^2}\sqrt{B^2 \Delta A^2 + A^2 \Delta B^2}. \tag{C3}$$

Finally, by replacing A, B, z, the uncertainty of experimental slip length, $\Delta\beta_{exp}$, becomes

$$\therefore \Delta\beta_{exp} = \frac{3}{\left(4\bar{u}_{H-P} - \bar{u}_{slip}\right)^2}\sqrt{\bar{u}_{H-P}^2 \Delta\bar{u}_{slip}^2 + \bar{u}_{slip}^2 \Delta\bar{u}_{H-P}^2}. \tag{C4}$$

The percentages of these uncertainties are shown by the error bars in Fig. 11.

[1] J. R. Philip, "Flows satisfying mixed no-slip and no-shear conditions," Z. Angew. Math. Phys. **23**, 353–372 (1972).
[2] J. R. Philip, "Integral properties of flows satisfying mixed no-slip and no-shear conditions," Z. Angew. Math. Phys. **23**, 960–968 (1972).
[3] E. Lauga and H. A. Stone, "Effective slip in pressure-driven Stokes flow," J. Fluid Mech. **489**, 55–77 (2003).
[4] J. Ou, B. Perot, and J. P. Rothstein, "Laminar drag reduction in microchannels using ultrahydrophobic surfaces," Phys. Fluids **16**, 4635–4643 (2004).
[5] P. Joseph, C. Cottin-Bizonne, J. M. Benoit, C. Ybert, C. Journet, P. Tabeling, and L. Bocquet, "Slippage of water past superhydrophobic carbon nanotube forests in microchannels," Phys. Rev. Lett. **97**, 156104 (2006).
[6] R. Truesdell, A. Mammoli, P. Vorobieff, F. van Swol, and C. J. Brinker, "Drag reduction on a patterned superhydrophobic surface," Phys. Rev. Lett. **97**, 044504 (2006).
[7] N. V. Priezjev, A. A. Darhuber, and S. M. Troian, "Slip behavior in liquid films on surfaces of patterned wettability: Comparison between continuum and molecular dynamics simulations," Phys. Rev. E **71**, 041608 (2005).
[8] B. Woolford, D. Maynes, and B. Webb, "Liquid flow through microchannels with grooved walls under wetting and superhydrophobic conditions," Microfluid. Nanofluid. **7**, 121–135 (2009).
[9] C. Teo and B. Khoo, "Analysis of Stokes flow in microchannels with superhydrophobic surfaces containing a periodic array of micro-grooves," Microfluid. Nanofluid. **7**, 353–382 (2009).
[10] K. Watanabe, Y. Udagawa, and H. Udagawa, "Drag reduction of Newtonian fluid in a circular pipe with a highly water-repellent wall," J. Fluid Mech. **381**, 225–238 (1999).
[11] E. Lauga, M. P. Brenner, and H. A. Stone, "Microfluidics: The no-slip boundary condition," in *Handbook of Experimental Fluid Dynamics*, edited by J. Foss, C. Tropea, and A. L. Yarin (Springer, 2007), Chap. 19, pp. 1219–1240.
[12] R. S. Voronov, D. V. Papavassiliou, and L. L. Lee, "Review of fluid slip over superhydrophobic surfaces and its dependence on the contact angle," Ind. Eng. Chem. Res. **47**, 2455–2477 (2008).
[13] J. P. Rothstein, "Slip on superhydrophobic surfaces," Annu. Rev. Fluid Mech. **42**, 89–109 (2010).
[14] O. I. Vinogradova and A. V. Belyaev, "Wetting, roughness and flow boundary conditions," J. Phys.: Condens. Matter **23**, 184104 (2011).
[15] A. Cassie and S. Baxter, "Wettability of porous surfaces," Trans. Faraday Soc. **40**, 546–551 (1944).
[16] R. Wenzel, "Resistance of solid surfaces to wetting by water," Ind. Eng. Chem. **28**, 988–994 (1936).
[17] N. Kashaninejad, W. K. Chan, and N.-T. Nguyen, "Eccentricity effect of micropatterned surface on contact angle," Langmuir **28**, 4793–4799 (2012).
[18] M. A. Samaha, H. V. Tafreshi, and M. Gad-el-Hak, "Modeling drag reduction and meniscus stability of superhydrophobic surfaces comprised of random roughness," Phys. Fluids **23**, 012001-1–012001-8 (2011).
[19] A. V. Belyaev and O. I. Vinogradova, "Effective slip in pressure-driven flow past super-hydrophobic stripes," J. Fluid Mech. **652**, 489–499 (2010).
[20] Y. P. Cheng, C. J. Teo, and B. C. Khoo, "Microchannel flows with superhydrophobic surfaces: Effects of Reynolds number and pattern width to channel height ratio," Phys. Fluids **21**, 122004-1–122004-12 (2009).

[21] C. Ybert, C. Barentin, C. Cottin-Bizonne, P. Joseph, and L. Bocquet, "Achieving large slip with superhydrophobic surfaces: Scaling laws for generic geometries," Phys. Fluids **19**, 123601-1–123601-10 (2007).
[22] N. Anantharaju, M. V. Panchagnula, S. Vedantam, S. Neti, and S. Tatic-Lucic, "Effect of three-phase contact line topology on dynamic contact angles on heterogeneous surfaces," Langmuir **23**, 11673–11676 (2007).
[23] D. Öner and T. J. McCarthy, "Ultrahydrophobic surfaces. Effects of topography length scales on wettability," Langmuir **16**, 7777–7782 (2000).
[24] M. C. Salvadori, M. Cattani, M. R. S. Oliveira, F. S. Teixeira, and I. G. Brown, "Design and fabrication of superhydrophobic surfaces formed of microcavities," Appl. Phys. Lett. **96**, 074101-1–074101-3 (2010).
[25] C. Liu, "Rapid fabrication of microfluidic chip with three-dimensional structures using natural lotus leaf template," Microfluid. Nanofluid. **9**, 923–931 (2010).
[26] M. E. Steinke and S. G. Kandlikar, "Single-phase liquid friction factors in microchannels," Int. J. Therm. Sci. **45**, 1073–1083 (2006).
[27] N. Kashaninejad, W. K. Chan, and N.-T. Nguyen, "Fluid mechanics of flow through rectangular hydrophobic microchannels," in *ASME Conference Proceedings* (2011), pp. 647–655.
[28] M. K. Koopaee, M. Jahanmiri, and H. M. Zadeh, "Numerical investigation of drag reduction in microchannels with superhydrophobic walls consist of aligned and staggered microposts," in *International Proceedings of Computer Science and Information Technology* (2012), Vol. 33, pp. 104–109.